nature communications

Article

https://doi.org/10.1038/s41467-025-57946-9

Unraveling oxygen vacancy-driven catalytic selectivity and hot electron generation on heterointerfaces using nanostructured platform

Received: 19 June 2024

Accepted: 5 March 2025

Published online: 25 March 2025

Check for updates

Gyu Rac Lee[1,4], Kyoungjae Song[2,4], Doosun Hong[3,4], Juyoung An[1], Yujin Roh[2], Minyoung Kim[3], Donghun Kim[1,3] ✉, Yeon Sik Jung[1] ✉ & Jeong Young Park[2] ✉

Modulating the physicochemical properties of oxides is crucial to achieve efficient and desirable reactions in heterogeneous catalysis. However, their catalytic role is not clearly identified because unevenly distributed interfaces and close conjugation with metal catalysts may hinder distinguishing their contribution in complex random structures. Here, we demonstrate a model platform composed of well-aligned CeO_x nanowire arrays on Pt catalysts to observe their catalytic role systematically. Independently modulating the crystallinity and oxygen vacancy concentration of oxide nanowires, while preserving heterogeneous interfaces, enables quantitative analysis of their individual effects on partial oxidation selectivity, resulting in hot electron generation during methanol oxidation reactions. CeO_x treated with vacuum annealing on Pt exhibits 1.47- and 2.12-times higher selectivity to methyl formate and chemicurrent yield than CeO_x without annealing on Pt. Density-functional theory calculations reveal that the promoted charge transfer from the electron-accumulated interface driven by oxygen vacancy acts as a key parameter in enhancing selectivity.

In multi-path chemical reactions, it is difficult to achieve high selectivity for a specific product simultaneously with a high reaction rate, because there is a trade-off between activity and selectivity[1,2]. The gas-phase methanol oxidation reaction (MOR), which is a representative multi-path reaction, can produce not only methyl formate (MF) but also CO_2 by partial oxidation and full oxidation, respectively[3]. Given the wide usage of MF as a feedstock for producing numerous high-value carbon products in the industry, the energy conversion of methanol to MF has gained great attention in C1 chemistry[4–6]. Therefore, the primary goal of MOR is to improve the partial oxidation selectivity for MF while minimizing the formation of CO_2.

Recently, it was demonstrated that in-situ measurement of catalytic selectivity in MOR is feasible through the detection of the quantity of generated energetic electrons (i.e., hot electrons), manifesting as chemicurrent[4,7]. As external energy accumulates on the metal catalyst during MOR, which is an exothermic reaction, energy conversion occurs via non-adiabatic processes (e.g., electron-hole pair excitation, chemiluminescence, and exo-emission) and adiabatic vibration (e.g., phonon)[8–11]. Among the energy dissipation processes, due to the

[1]Department of Materials Science and Engineering, Korea Advanced Institute of Science and Technology, 291 Daehak-ro, Yuseong-gu, Daejeon, Republic of Korea. [2]Department of Chemistry, Korea Advanced Institute of Science and Technology, 291 Daehak-ro, Yuseong-gu, Daejeon, Republic of Korea. [3]Computational Science Research Center, Korea Institute of Science and Technology, 14-gil 5, Hwarang-ro, Seongbuk-gu, Seoul, Republic of Korea. [4]These authors contributed equally: Gyu Rac Lee, Kyoungjae Song, Doosun Hong. ✉e-mail: donghun@kist.re.kr; ysjung@kaist.ac.kr; jeongypark@kaist.ac.kr

significantly lower heat capacity of electrons than lattice[12], electronic excitation can generate hot electrons that are not in thermal equilibrium with metal atoms[13–15]. However, as hot electrons decay via scattering of electron-phonon and electron-electron in ultrafast time (~fs), detecting hot electrons has been proven challenging[8,16]. Especially, Schottky nanodiodes, which have the potential barrier (i.e., Schottky barrier) at the interface between metal and semiconductor, enable the prompt collection of hot electrons[9,17]. As only hot electrons with sufficient energy (1-3 eV) can overcome the Schottky barrier, the electrons promptly flow from the metal to the semiconductor enabling the selective detection of these electrons before recombination. In this regard, Schottky nanodiodes can be utilized as a powerful and convenient in-situ technique to estimate catalytic selectivity.

In the pursuit of enhancing partial oxidation selectivity in MOR, forming heterogeneous interfaces by incorporating active noble metals on metal oxide supports has become a prevalent approach[4,18,19]. This trend is driven by the strong metal-support interaction (SMSI), which originates from charge transfer through metal-oxide interfaces, and acts as a catalytic promoter[20,21]. Several studies in various fields including MOR already revealed that the metal-oxide interface plays an important role in improving overall catalytic performance[22–25]. Especially, the density of the metal-oxide interface is largely responsible for determining the degree of catalytic improvement, which can be manipulated quantitatively by utilizing well-aligned nanowire arrays with different widths and periods, as our group previously reported[4]. In addition to the metal-oxide interface, modulating inherent characteristics of metal oxides such as crystallinity, which gives well-formed and evenly distributed active sites compared to the amorphous state[26], is also a key strategy for augmenting selectivity. Recent studies have argued that it is necessary to optimize the physicochemical properties of metal oxides thoroughly to maximize the enhancement of performance[27–29]. However, the underlying influence and role of each variable on heterogeneous catalysis remain unclear, because it is challenging to differentiate their own contribution toward overall catalytic performance from other prominent factors.

In conventional heterogeneous systems with random structures, the structural complexity and uneven distribution of metal-oxide interfaces may hinder quantitative analysis. Furthermore, in such random structures, reaction sites—particularly interfaces—are often not fully utilized due to the agglomeration or coarsening of active materials, which can lead to an underestimation of the overall catalytic performance[30,31]. The close correlation between metal catalysts and metal oxides also poses a significant bottleneck for quantitative analysis[29]. When the physicochemical properties of metal oxide are modulated, the properties of metal catalysts also change simultaneously, making it difficult to modify a specific parameter individually. Although a few studies successfully elucidated the innate effects of the size and type of materials on catalytic performance specifically through systematically controlled environments, these are limited to modifying only the morphological factors of metal catalysts[25]. Therefore, these challenges propose the necessity of developing an ideal platform that provides both highly ordered structures and independent tunability of metal oxide properties.

To address these issues, we demonstrate a novel heterogeneous platform utilizing well-aligned nanowire arrays, aiming to facilitate unprecedented quantitative analysis for distinguishing the contribution of each variable to catalytic performance. Based on CeO_x nanowire arrays formed on Pt catalysts (CeO_x/Pt), the inherent contribution of modulated-CeO_x properties to both partial oxidation selectivity and chemically-induced hot electrons was estimated. As a result, the crystallinity of CeO_x plays a critical role in enhancing both the reaction rate and MF selectivity. Interestingly, with the same crystalline state, CeO_x treated with vacuum annealing on Pt (Vac.-CeO_x/Pt) achieved significantly enhanced MF selectivity which is 1.35 times higher than CeO_x treated with O_2 annealing (O_2-CeO_x/Pt), thereby detecting many more excited hot electrons even with the similar reaction rate. Employing density-functional theory (DFT) analysis, we reveal that the improvements in MF selectivity are associated with the reduction of the activation barrier driven by a high fraction of oxygen vacancy in the Vac.-CeO_x/Pt, which leads to efficient charge transfer to reaction intermediates.

Results

Fabrication and characterization of CeO_x nanowire arrays

We have integrated the CeO_x nanowire arrays with modulated physicochemical properties and Pt film as a model heterogeneous system to precisely elucidate their role on catalytic performance, especially MF selectivity toward MOR. Two different methods are utilized to evaluate the catalytic performance: sensing signal and electrical signal. Particularly, the Schottky barrier between TiO_2 and Pt was formed by fabricating this model system on top of the TiO_2 layer to detect reaction-induced hot electrons which enables real-time detection of catalytic performance, as depicted in Fig. 1. First, CeO_x nanowire arrays with modified physicochemical properties were fabricated using solvent-assisted nanotransfer-printing (S-nTP)[31–35], the method that our group reported previously, with an additional high-temperature annealing process, as shown in Fig. 2a. Through the S-nTP process, uniformly aligned nanowire arrays with a width of 25 nm, a pitch of 25 nm, and a thickness of 20 nm were prepared on a target substrate, as presented in the scanning electron microscopy (SEM) image in Fig. 2b. This ultrahigh-resolution patterning of nanowires enhances the density of the heterogeneous interfaces, which provides a remarkable improvement of catalytic selectivity, as demonstrated in our previous research[4]. After the transfer-printing process, the pristine CeO_x nanowire arrays were annealed at 500 °C for 2 hours under various atmospheres: vacuum, Ar, and O_2. The temperature and time for the annealing process are sufficient to fully crystallize the CeO_x nanowires[36]. As shown in Fig. 2b and Supplementary Fig. 1, the overall morphologies of the CeO_x nanowire arrays such as shape and alignment were retained after annealing, regardless of the conditions, maintaining the density of heterogeneous interfaces. Therefore, by fixing the density of interfaces, the contribution of modified properties of metal oxide during annealing toward enhanced catalytic performance can be precisely estimated through comparison among these samples.

During the annealing process, two main characteristics of the CeO_x nanowire arrays can be modulated: crystallinity and oxidation states. First, to examine the crystallinity, transmission electron microscopy (TEM) analysis (Fig. 2c) and X-ray diffraction (XRD) analysis (Fig. 2d) were conducted. As shown in Fig. 2c, the CeO_x nanowire treated with vacuum annealing was transformed to aggregates with a number of nanoscale grains in crystalline states. The XRD spectra suggest that the pristine CeO_x nanowire arrays have an amorphous state due to the nature of e-beam evaporation[33]. However, the XRD spectra of the annealed samples exhibited sharp and narrow diffraction peaks assigned to the crystal planes of cerium oxide, indicating the enhancement of crystallinity. Thus, the influence of amorphous and fully crystalline states on catalytic performance can be elucidated by analyzing the difference between pristine and annealed CeO_x. The oxidation states of the CeO_x nanowire arrays were examined by X-ray photoelectron spectroscopy (XPS). The deconvolution of the Ce *3d* peaks into Ce $3d_{5/2}$ and Ce $3d_{3/2}$ was carried out to analyze the ratio between Ce (III) and Ce (IV) according to the annealing conditions (Supplementary Fig. 2). As shown in Fig. 2e, the ratio of Ce (III) in the CeO_x nanowire arrays treated with vacuum annealing increased to 46.69%, which is 1.85 times higher than the 25.22% ratio obtained with O_2 annealing. Compared to the pristine CeO_x sample, which exhibited a Ce (III) portion of 32.21%, reducing and oxidizing conditions give rise to higher and lower ratios of Ce (III) states, respectively. The formation of oxygen vacancies accompanies the formation of electrons, which

https://doi.org/10.1038/s41467-025-57946-9

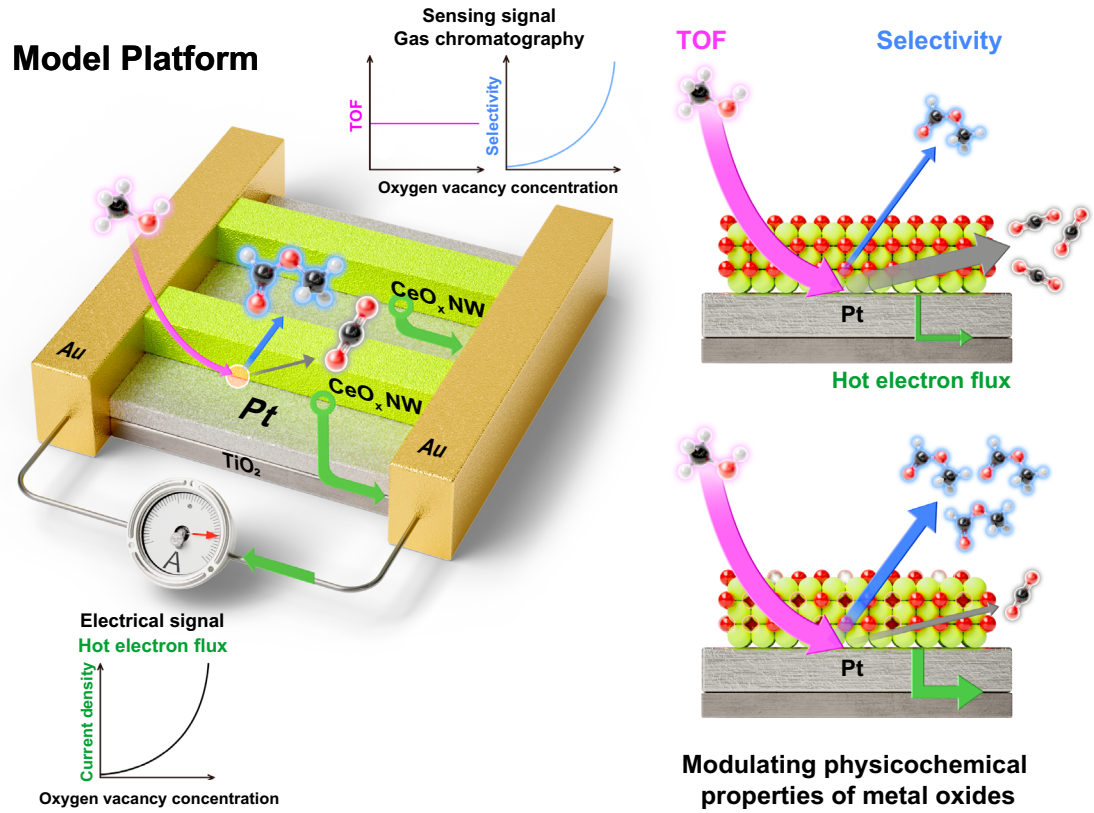

Fig. 1 | Schematic illustration of a model heterogeneous platform composed of CeO_x nanowire arrays with modulated physicochemical properties on Pt catalysts (CeO_x/Pt) for an accurate analysis of their role and influence on methyl formate (MF) selectivity toward methanol oxidation reaction (MOR). Two different methods are utilized to evaluate the partial oxidation selectivity of each catalyst: electrical signal (hot electron flux) using ammeter and sensing signal (Turnover frequency and MF detection) using gas chromatography. Crystallinity gives well-formed and evenly distributed active sites that can enhance both reaction rates and MF selectivity compared to the amorphous state. Moreover, the oxygen vacancies within the ceria induce electron accumulation at the heterogeneous interfaces and as a result, supply more electrons to the reactant molecules for alkoxy hemiacetal formation. Therefore, the activation barrier for alkoxy hemiacetal formation is reduced, leading to highly improved MF selectivity, thereby generating enhanced hot electron flux.

leads to a reduction in the oxidation state. Thus, the controlled oxidation states in each CeO_x sample, achieved through the formation and filling of oxygen vacancies[37,38], aimed at identifying the effects of the oxygen vacancy concentration on catalytic performance quantitatively. Moreover, we conducted an additional analysis to verify and support our XPS results using Raman spectroscopy. The relative oxygen vacancy concentration can be compared by calculating the intensity ratio between the CeO_2 band at 460 cm^{-1} and the oxygen vacancy band at 546 cm^{-1} in the Raman spectra[39]. As shown in the Raman spectra (Supplementary Fig. 3a), the intensity of the CeO_2 band (460 cm^{-1}) and the oxygen vacancy (O_v) band (546 cm^{-1}) vary significantly depending on the annealing conditions. The intensity ratio of the O_v band to the CeO_2 band under different annealing conditions is plotted in Supplementary Fig. 3b. Notably, the trend of the O_v/CeO_2 intensity ratio achieved from Raman spectra aligns with the Ce (III) ratio obtained from the XPS analysis (Fig. 2e).

Finally, the multiple types of CeO_x nanowire arrays were individually transferred on a Pt film (CeO_x/Pt) to form heterogeneous catalysts for evaluating MOR performance (Supplementary Fig. 4). The interfaces with Pt film form later, regardless of the annealing conditions, so the possibility of strain effects[40], which can influence the catalytic performance, can be ruled out. This model platform, designed with sophisticatedly controlled environments, is intended for the effective and accurate verification of how the modified properties of CeO_x nanowires influence MOR performance and to distinguish their innate contributions from various parameters. A more detailed analysis to evaluate the MOR performance, especially partial oxidation selectivity and reaction-induced hot electron flux, is discussed in the next section.

Detection of hot electrons generated on CeO_x/Pt catalysts through Schottky nanodiodes

For a real-time detection of hot electrons generated from MOR, catalytic nanodiodes were designed, as illustrated in Fig. 3a. The nanodiode consists of Au/Ti electrodes for Ohmic contact to form an electrical circuit, CeO_x/Pt as a catalyst of MOR, and TiO_2 support for a formation of Schottky barrier at the interface between Pt film and TiO_2. As presented in the inset of Fig. 3a, the device has the dense and uniform CeO_x-Pt interfaces, where the catalytic reaction occurs mainly, through well-aligned structures. Figure 3b visualizes the energy band diagram of the catalytic nanodiode and the designed working principles of hot electron generation under MOR conditions. The exothermic reaction energy of MOR generates hot electrons through nonadiabatic electron excitation at metal-oxide interfaces. Consequently, only electrons with sufficient energy to overcome the Schottky barrier can be injected into the conduction band of n-type TiO_2, facilitating current flow.

To confirm electrical characteristics and rectifying behavior, current-voltage (*I-V*) characteristics of the catalytic nanodiodes were obtained. As illustrated in Fig. 3c, the Schottky barrier heights for the nanodiodes with various CeO_x/Pt catalysts were determined by fitting the current-voltage (*I-V*) characteristics to the Richardson-Dushman equation. (Supplementary Note 1, Supplementary Table 1). As depicted in the inset figure, the *I-V* curve for the nanodiode comprising a Pt film on TiO_2 without CeO_x nanowire arrays demonstrates the rectifying behavior characteristic of Schottky nanodiodes, suggesting the perfectly effective formation of the nanodiode[13]. Both the ideality factor and Schottky barrier height in Pt-TiO_2 were obtained as 1.35 and 0.835 eV, respectively. It is already known that the Schottky barrier height

https://doi.org/10.1038/s41467-025-57946-9

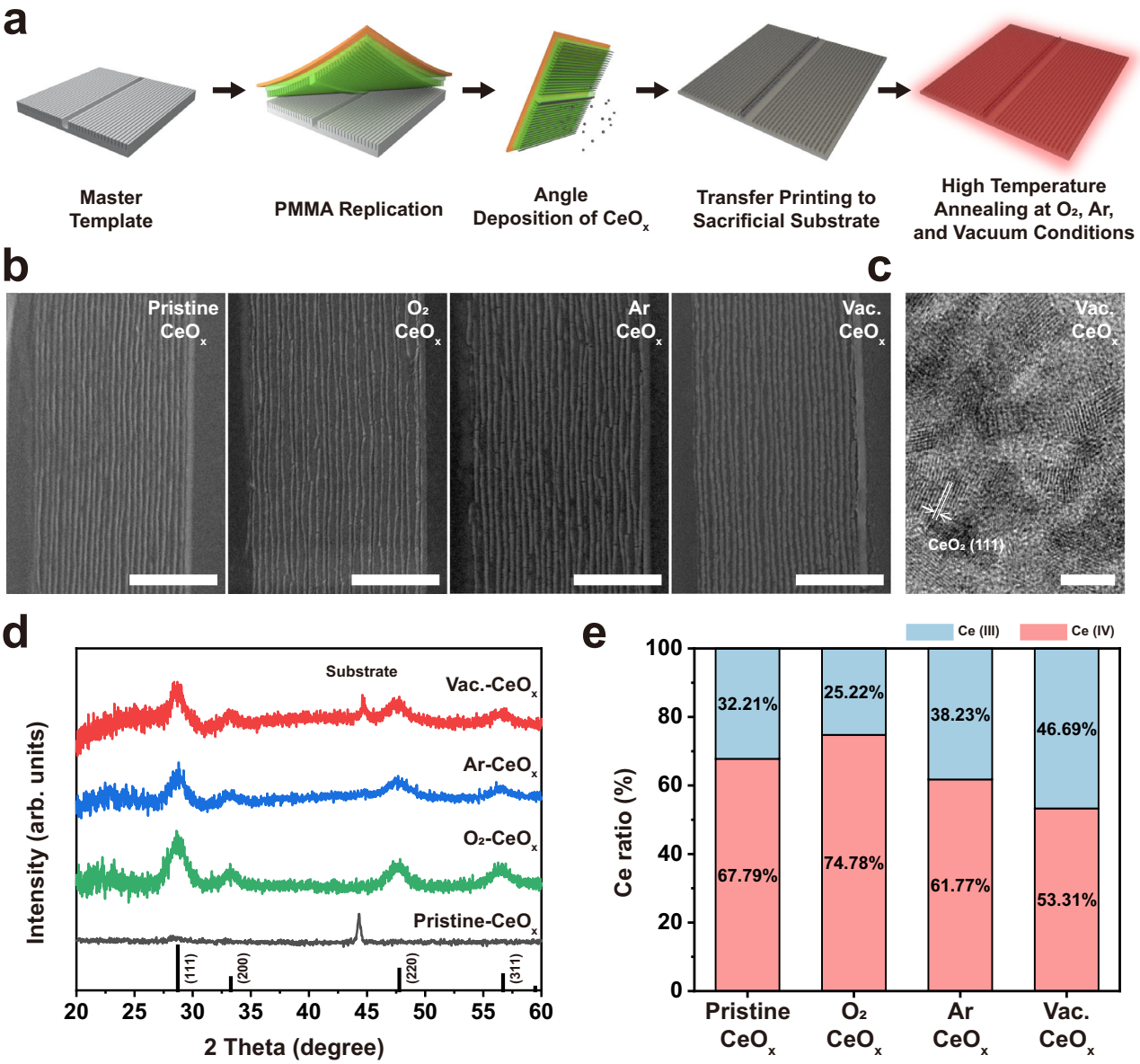

Fig. 2 | Fabrication and characterization of CeO_x nanowire arrays with modified physicochemical properties. a Schematic illustration of the fabrication process of physicochemical properties modulated CeO_x nanowire arrays through solvent-assisted nanotransfer printing method combined with high-temperature annealing in various conditions: vacuum, Ar, and O_2 atmosphere. **b** SEM images of the pristine CeO_x nanowire array without annealing and CeO_x nanowire arrays annealed with various conditions (as indicated) for 2 hours at 500 °C (scale bar, 500 nm). **c** TEM image of the CeO_x nanowire treated with vacuum annealing (scale bar, 5 nm). **d** XRD spectra of the pristine CeO_x nanowire arrays which have an amorphous state and CeO_x nanowire arrays treated with various annealing conditions which have a polycrystalline state. **e** Characterization of the oxidation states of pristine CeO_x nanowire arrays and CeO_x nanowire arrays treated with various annealing conditions by using XPS.

between Pt and TiO_2 is 0.76–0.87 eV[7,41], indicating that the Schottky junction at Pt-TiO_2 was well established. As shown in Fig. 3c and Supplementary Fig. 5, all the CeO_x/Pt/TiO_2 Schottky nanodiodes exhibited a negligible difference in Schottky barrier height compared to nanodiode without CeO_x nanowire arrays, indicating that the deposition of CeO_x nanowires on Pt/TiO_2 nanodiode does not affect the interface at Pt/TiO_2 because the CeO_x was physically deposited on the surface of Pt film. Consequently, the results confirmed that, due to the intact interfacial junction at Pt/TiO_2, the negligible difference in Schottky barrier height does not influence the flux of hot electrons in this study. Furthermore, through XPS analysis, it was confirmed that the chemical states of Pt, which can affect the catalytic performance, are almost invariant across all CeO_x/Pt nanodiodes (Supplementary Fig. 6).

To measure the flux of hot electrons, the difference in current density under MOR conditions (4 Torr of methanol vapor mixed with 756 Torr of O_2, at temperatures ranging from 323 to 353 K) and under non-reaction conditions (pure O_2 at 760 Torr, within the same temperature range) was determined using an ammeter as the current detector in an open circuit system. Under the non-reaction condition, a negligible thermoelectric current was measured, due to the electrical potential difference between the two electrodes, known as the Seebeck effect[42] (Supplementary Fig. 7). The current density under the MOR condition exhibits an apparent enhancement compared to the non-reaction condition. This implied that the enhanced current signals can be attributed to the hot electron flux based on the catalytic reaction.

As shown in Fig. 3d, the chemicurrent density of each sample, depending on annealing conditions and temperature, was obtained. When the reaction temperature is elevated, the chemicurrent density of all CeO_x/Pt catalytic nanodiodes is enhanced,

https://doi.org/10.1038/s41467-025-57946-9

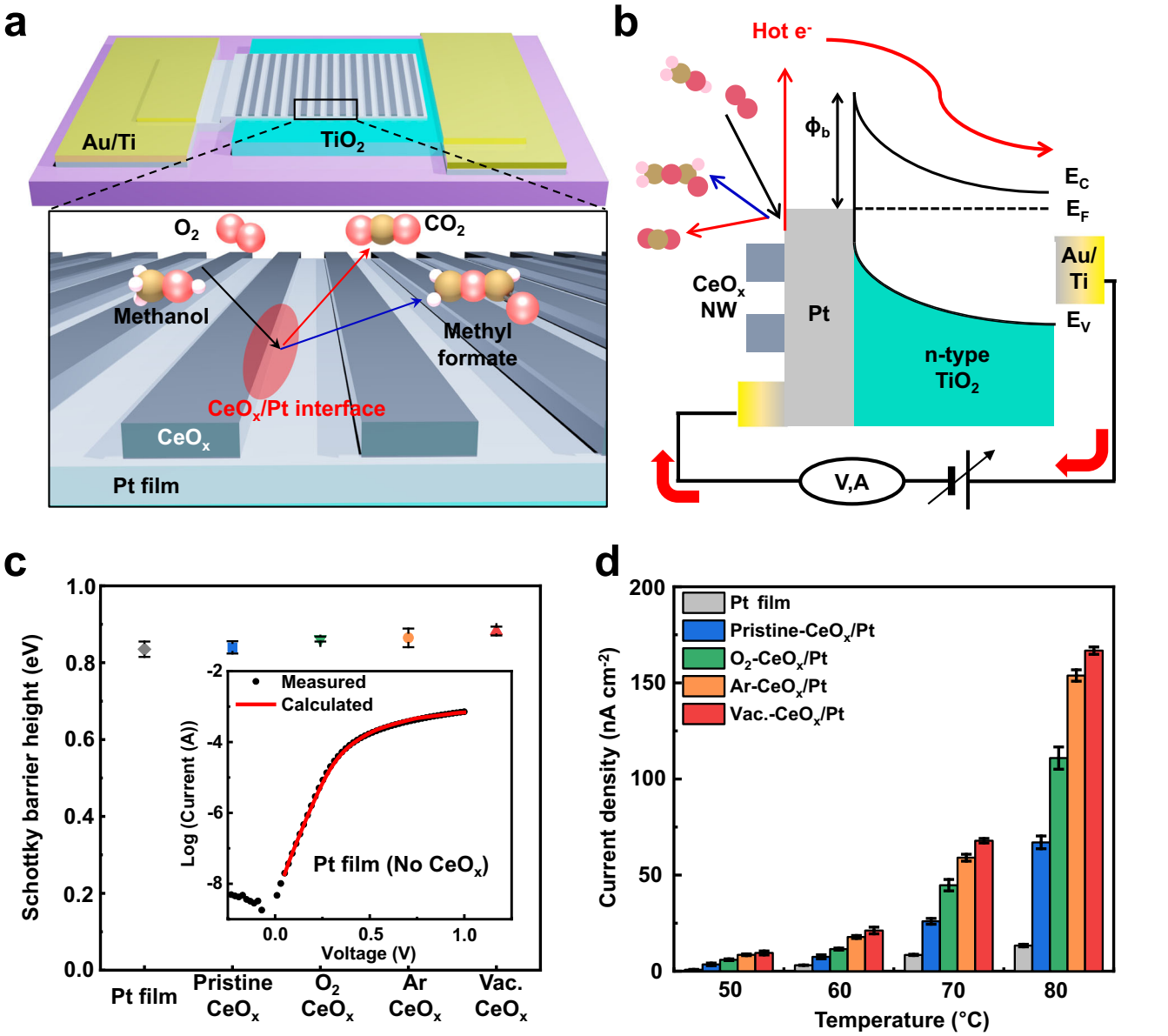

Fig. 3 | Detection of hot electrons generated on CeO_x/Pt nanodiodes. a Scheme of CeO_x/Pt film/TiO_2 Schottky nanodiodes that can detect the hot electron flux from methanol oxidation reaction (MOR). MOR strongly occurs at the CeO_x-Pt interface producing the methyl formate and CO_2 gas. **b** Energy band diagram of the Schottky nanodiode. Hot electrons from exothermic MOR at CeO_x-Pt interface can be detected as steady-state current signals when the hot electrons with excess energy overcome the Schottky barrier height. **c** Schottky barrier height of fabricated nanodiodes with independently modulated CeO_x nanowire arrays. The inset figure shows current-voltage curves of Pt-TiO_2. The red line means the curve that was calculated by the thermionic emission equation. **d** Current density difference between under MOR (a mixture of methanol 4 Torr and oxygen 756 Torr) and under non-reactive condition (oxygen 760 Torr) according to temperature.

implying that the current signals are affected by the heightened catalytic activity as a function of the reaction temperature. Furthermore, the CeO_x/Pt nanodiodes show a significantly enhanced current density by a factor of 6–10 compared to the reference Pt film nanodiode, which confirms that the Pt-CeO_x interfaces have an impact on the hot electron flux under exothermic methanol oxidation. It is noteworthy that the Vac.-CeO_x/Pt exhibited ~2.5 times and 1.6 times higher chemicurrent density at 353 K compared to the CeO_x without annealing on Pt (Pristine-CeO_x/Pt) and O_2-CeO_x/Pt, respectively.

Given that the chemical states of Pt are similar, the variations in the crystallinity and oxygen vacancy concentrations of CeO_x nanowire arrays may impact the amount of excited hot electrons under MOR. The detection of hot electrons using a model heterogeneous system can precisely distinguish the intrinsic contribution of the modified physicochemical properties on MOR. Specifically, the crystalline state and low oxidation states in CeO_x nanowires led to a boost in hot electron generation. All catalytic nanodiodes exhibited stable steady-state current signals, owing to their excellent thermal and electrical stability under the MOR environment (Supplementary Fig. 8).

Analyzing the MOR selectivity of CeO_x/Pt catalysts

To investigate the effects of CeO_x with modulated properties on catalytic performance, the MOR was conducted in a batch reactor, while reaction-induced hot electrons were measured using the Schottky nanodiodes. Recently, it has been observed that the different oxidation states of metal oxides could lead to enhanced partial oxidation selectivity in MOR[43,44]. However, it remains a challenge to separate their own impact from other parameters in typical random catalyst

https://doi.org/10.1038/s41467-025-57946-9

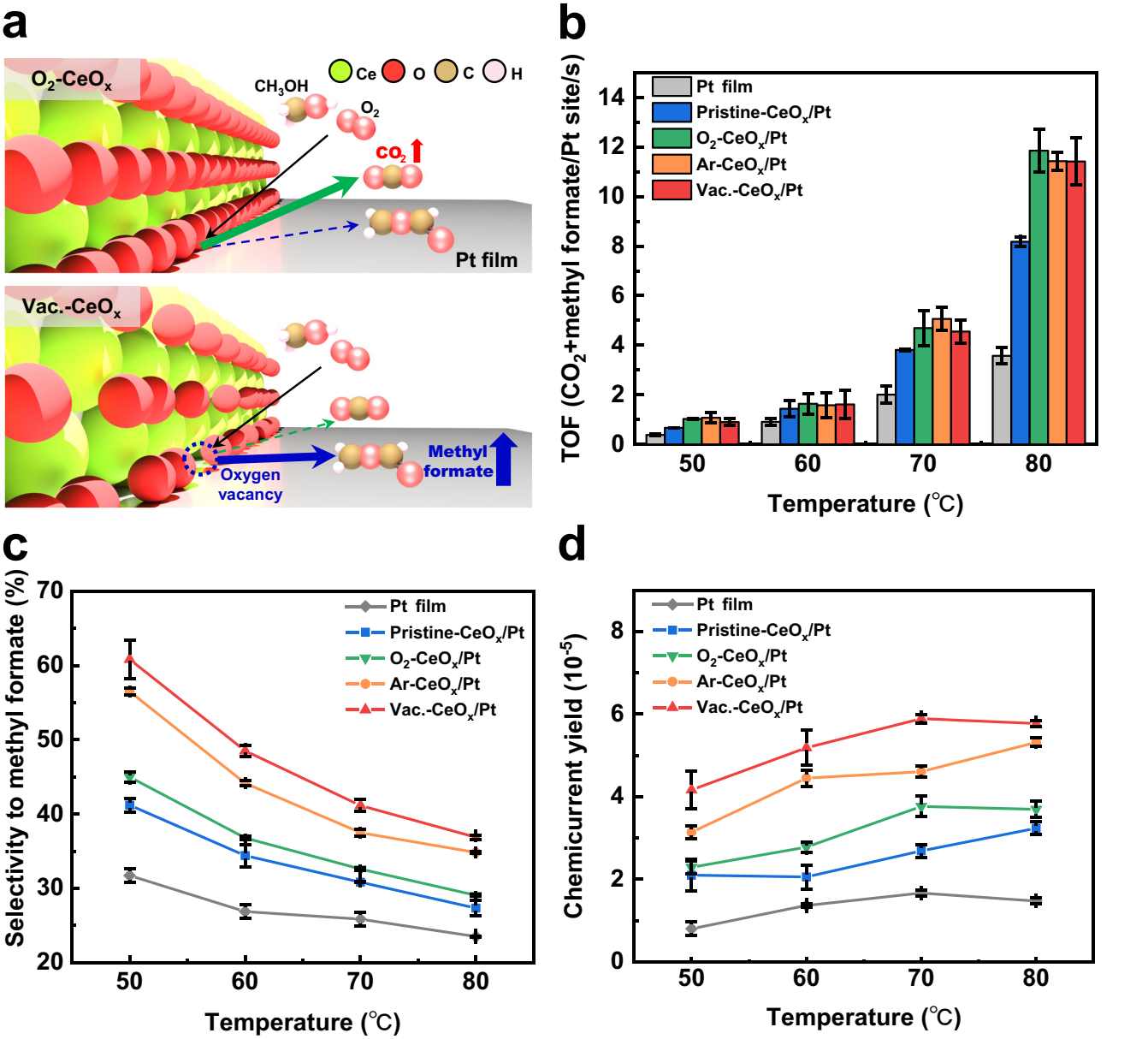

Fig. 4 | Catalytic selectivity and chemicurrent yield of CeO_x/Pt nanodiodes. **a** Schematic illustration of O_2-CeO_x/Pt (upper image) and Vac.-CeO_x/Pt (below image). The high Ce (III) ratio induced by oxygen vacancy formation can control the selectivity of methanol oxidation reaction. The green, red, brown, and pink balls indicate Ce, O, C, and H, respectively. **b** Total TOFs and **c** selectivity of methyl formate formation during methanol oxidation depending on temperature. **d** Chemicurrent yield calculated from the total TOF and chemicurrent density. The yield indicates the hot electron generation efficiency measured from the CeO_x/Pt nanodiodes under methanol oxidation environment.

systems. Figure 4a illustrates the reaction pathway of the MOR as a function of the oxygen vacancy concentration of CeO_x nanowire arrays on Pt film. Turnover frequencies (TOF) for reaction products were calculated by fitting the slope of turnover number (TON) depending on reaction time (Supplementary Fig. 9). Every TOF was obtained under the methanol conversion of 20%.

Figure 4b shows total TOFs, which indicate the sum of the TOFs of MF and CO_2 during MOR. The total TOFs for various CeO_x/Pt catalysts were, on average, improved by a factor of 2.52 compared to the total TOFs of bare Pt film. Moreover, the comparison between the Pristine-CeO_x/Pt and annealed samples presents an average improvement of 1.33 times due to annealing. These results clearly suggest that the total reactivity of MOR is associated with the metal-oxide interfaces and the crystallinity of CeO_x nanowire arrays. However, all the CeO_x/Pt catalysts exhibited similar total TOFs, implying that the different oxygen stoichiometry in CeO_x nanowire arrays did not affect the total reaction activity of MOR.

The selectivity of partial oxidation described in Fig. 4c was obtained by the reaction ratio of MF per total reaction products. As the reaction temperature was elevated, the selectivity for MF formation was reduced, indicating that CO_2 formation exhibited a higher activation energy barrier than MF formation[45]. There is a clear enhancement on partial oxidation selectivity in Vac.-CeO_x/Pt compared to Pristine-CeO_x/Pt and bare Pt film catalysts (e.g., 60.82%, 41.19%, and 31.71% at 323 K, respectively). Interestingly, the Vac.-CeO_x/Pt exhibited 1.35 times higher MF selectivity compared to O_2-CeO_x/Pt. Annealing CeO_x nanowire arrays under vacuum conditions led to a reduction in the oxidation state of Ce, thereby increasing the presence of oxygen vacancies within CeO_x. The findings suggest that while the increase in oxygen vacancies within CeO_x nanowire arrays does not alter the

overall reactivity for MOR, it significantly enhances the selectivity towards partial oxidation.

Efficiency of hot electron generation on CeO_x/Pt nanodevices

To further elucidate the critical role of modified physicochemical characteristics, we extracted the generation efficiency of hot electrons by using the total TOF and chemicurrent results. Because the current signals from hot electron flux under reaction conditions are proportional to reaction activity[46], the chemicurrent density on CeO_x/Pt catalytic nanodiodes can be expressed as Eq. (1)

$$I = \alpha q A N_{Pt} \mathrm{TOF} \quad (1)$$

where $\alpha, q, A, N_{Pt,}$ and TOF indicate a chemicurrent yield, elementary charge, active area on the Pt film, the number of Pt sites per square centimeter, and a turnover frequency of methanol oxidation, respectively[47]. The N_{Pt} values were calculated by an assumption that the surface density of Pt film is equivalent to the density of Pt (111) sites. Thus, the chemicurrent yield, which means the number of captured hot electrons per one molecule of a product under methanol oxidation, can be obtained from the above equation. Figure 4d shows the efficiency of hot electron generation, known as chemicurrent yield, depending on the annealing conditions and reaction temperature. Pt film nanodiode, which has no interfaces, exhibited the lowest yield of hot electrons due to the lowest total TOF and selectivity to partial oxidation. In contrast, the yields of hot electrons in CeO_x/Pt catalysts clearly improved because the chemicurrent yield, corresponding to previous studies, was closely associated with enhanced TOF[48] and selectivity of MF formation[4]. At a reaction temperature of 323 K, the chemicurrent yield of Vac.-CeO_x/Pt is almost 2 and 5 times higher compared to Pristine-CeO_x/Pt and bare Pt film, respectively. This demonstrated that the formation of Pt-CeO_x interfaces, along with enhanced crystallinity, governed hot electron generation by increasing both the total reactivity and the selectivity for partial oxidation.

Furthermore, the highest chemicurrent yield was achieved with the value of 4.17×10^{-5} in Vac.-CeO_x/Pt, which is a 1.82-fold improvement on average compared to O_2-CeO_x/Pt. This implies that the enhancement in MF production affects the generation of hot electrons, which is well-matched with previous research[7]. Notably, the ratio of Ce (III) in Vac.-CeO_x /Pt was 1.85 times higher than that of O_2-CeO_x/Pt, confirming that the efficient generation of hot electrons is associated with the density of oxygen vacancies in CeO_x nanowire arrays. This is supported by the results of chemicurrent yield and deconvolution of XPS in CeO_x/Pt catalysts (Supplementary Fig. 2). Thus, these results conclusively demonstrate that the modified CeO_x in a crystalline state and low oxidation states can govern the production of partial oxidation under methanol oxidation and thereby generate hot electrons more efficiently.

Origin of the enhanced selectivity of methyl formate on Vac.-CeO_x/Pt system

Additionally, to gain further insight into the enhanced selectivity of MF on Vac.-CeO_x/Pt interface compared to CeO_2/Pt, DFT calculations were performed. As depicted in Fig. 5a, three systems are modeled, which include Pt(111), CeO_2/Pt(111), and Vac.-CeO_x/Pt(111). CeO_2 and CeO_x parts are modeled in tetrahedral cluster form rather than nanowire form in the simulations to avoid the issues of undesirable lattice strains between ceria and Pt. The cluster of CeO_2 consists of 10 cerium atoms and 20 oxygen atoms ($Ce_{10}O_{20}$), which is stable, moderate-sized, and well aligned on Pt(111) slab of ~100 Pt atoms[49]. The cluster of CeO_x was made by generating two oxygen vacancies at the interface of Pt and ceria, and the stoichiometry (Ce and O) was determined based on the experimental measurements.

The reaction profiles of methanol oxidations to form MF are well documented in literature[4,7,50,51], which suggests four sequential reaction steps as governing steps including (1) $*CH_3OH + *O \rightarrow *CH_3O + *OH$, (2) $*CH_3O + *OH \rightarrow *CH_2O + *H_2O$, (3) $*CH_3O + *CH_2O \rightarrow *CH_3OCOH_2$ (*aka* alkoxy hemiacetal formation), and last, (4) $*CH_3OCOH_2 + *OH \rightarrow CH_3OCOH_{(g)} + H_2O_{(g)}$. For three modeling systems of Pt(111), CeO_2/Pt(111), and Vac.-CeO_x/Pt(111), the energetics for these four reaction steps were computed, and the results are shown in Fig. 5b and Supplementary Table 2. The energetics for reactions (1) and (2) were observed overall similarly regardless of the presence of either ceria cluster itself or vacancies within the cluster, which indicates that these two reaction steps are the least influential in explaining the experimental observations. In contrast, noticeably large differences in the reaction barrier were found between three modeling systems for the alkoxy hemiacetal formation where O-C coupling is mainly involved. In particular, the barrier for Vac.-CeO_x/Pt(111) was only 0.032 eV, which is substantially smaller than 0.398 eV for CeO_2/Pt(111) and 0.634 eV for Pt(111) system. This trend of the reaction barrier for the alkoxy hemiacetal formation agrees with experimental observations of the much-enhanced selectivity of Vac.-CeO_x/Pt system. In the last dehydration step of reaction (4), the presence of ceria cluster itself significantly lowers the barrier, while the vacancy generations within the cluster barely affect the barrier.

It is important to note that CH_2O, an intermediate in the oxidation of methanol, can follow two competitive pathways: alkoxy hemiacetal formation leading to partial oxidation into methyl formate and additional dehydrogenation resulting in full oxidation to CO_2. The latter pathway, which can be described by the reaction $*CH_2O + *OH \rightarrow *CHO + H_2O_{(g)}$ is detailed in Supplementary Table 3. Our studies have shown that in the Vac.-CeO_x/Pt(111) system, the alkoxy hemiacetal formation is energetically more favorable than the competing pathway. Conversely, in the CeO_x/Pt(111) and pure Pt(111) systems, the opposite trend is observed. These findings support the critical role of the vacancy formation within ceria in selectively promoting the formation of methyl formate rather than CO_2.

The introduction of ceria clusters on Pt slab (thereby, producing heterogeneous system) indeed lowers the barriers for the alkoxy hemiacetal formation compared to pure Pt system. This finding was similarly reported in our previous study[4] of Pt nanorod on TiO_2, and results from the different adsorption configurations of CH_2O (formaldehyde). For pure Pt, both C and O of CH_2O are bonded to the surface, whereas for ceria/Pt hybrid systems, only O of CH_2O is bonded to the surface, which thereby does not require the breaking of metal-C bonding and facilitates the corresponding reaction.

The vacancy formation within the ceria cluster (CeO_2/Pt(111) → Vac.-CeO_x/Pt(111)) substantially lowers the barriers for the alkoxy hemiacetal formation, and this finding can be understood based on the charge redistribution behaviors between two systems (Fig. 5c). It was observed that the oxygen vacancies result in more electron accumulations at the heterogeneous interface of Vac.-CeO_x/Pt(111), and as a result supply more abundant electrons (additional 0.12 e^- compared to the system without O vacancies) to the reactant molecules of $*CH_2O$ and $*CH_3O$. For the alkoxy hemiacetal formation reaction to take place, the C atom in $*CH_2O$ must bond with the O atom in $*CH_3O$ (Supplementary Figs. 11, 12). The gain of these additional electrons appears to play an important role in promoting the alkoxy hemiacetal formation since they help stabilize O-C bond formation. To quantitatively confirm the effect of additional electrons, we performed slow-growth ab-initio molecular dynamics (AIMD) as described in Supplementary Fig. 13, where the quantity of additional electrons was forcefully controlled within reactant molecules without the catalyst materials being present. Indeed, in the AIMD result, the addition of more electrons to reactants tends to reduce the barriers by facilitating the O-C bond formation.

https://doi.org/10.1038/s41467-025-57946-9

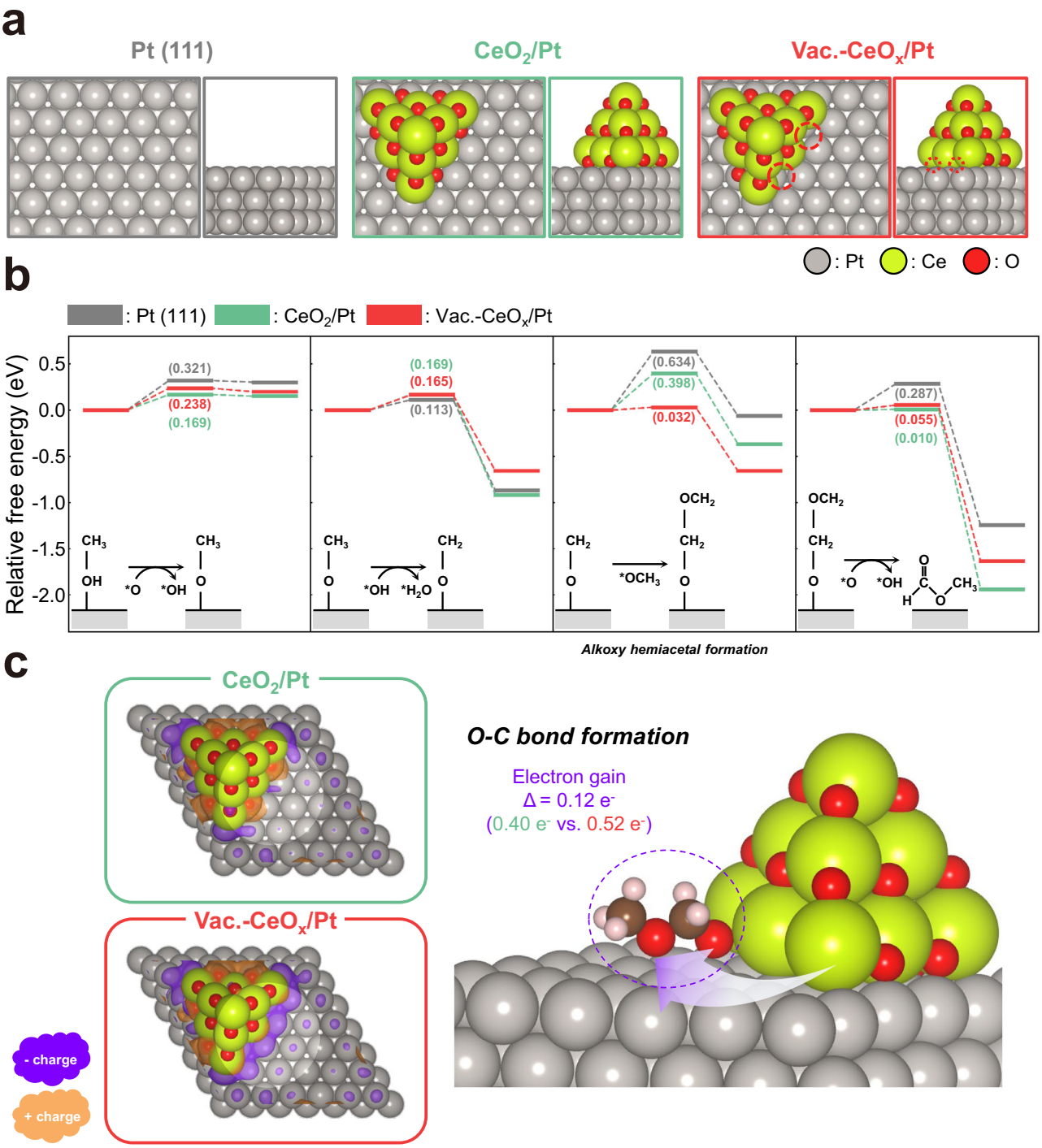

Fig. 5 | DFT calculation results of methanol oxidation reactions for Pt(111), CeO_2/Pt, and Vac.-CeO_x/Pt. a Structural descriptions (top and side views) of three modeling systems. Tetrahedral $Ce_{10}O_{20}$ and $Ce_{10}O_{18}$ clusters are attached onto the Pt(111) to simulate the experimental systems of CeO_2/Pt and Vac.-CeO_x/Pt. Two oxygen vacancies are located at the interfacial area. **b** The free energy profiles of methyl formate production from methanol oxidation on three modeling systems. Numbers in parentheses represent the reaction barrier (in eV). **c** The comparisons of charge redistributions between CeO_2/Pt and Vac.-CeO_x/Pt. The left part figure of charge redistributions was produced based on the equation of $\Delta\rho = \rho_{total} - [\rho_{ceria\ cluster} + \rho_{Pt\ film}]$). The highlighted area is the heterogeneous interface where the primary charge redistribution occurs. The right part figure schematically shows the electron transfers from catalyst to reactant molecules of alkoxy hemiacetal formation reaction. The introduction of oxygen vacancies supplies more abundant electrons at the heterogeneous interface, which finally facilitates the formation of O-C bonds during the alkoxy hemiacetal formation. The green, red, gray, brown, and pink balls indicate Ce, O, Pt, C, and H, respectively.

Discussion

In summary, we successfully elucidated and established the intrinsic contribution of physicochemical properties of metal oxides on catalytic performance by investigating the partial oxidation selectivity and the reaction-induced hot electrons toward MOR. Using a model heterogeneous system composed of CeO_x nanowire arrays and Pt film, we identified that both the crystallinity and oxidation states of CeO_x have a significant influence on the overall MOR performance. The properties of CeO_x were modified separately by annealing with different atmospheres before forming metal-oxide interfaces with Pt film.

Then, fabricated CeO_x/Pt catalysts were deposited on TiO_2 to form Schottky nanodiodes. First, we confirmed that the formation of the metal-oxide interfaces in CeO_x/Pt enhanced partial oxidation selectivity, thereby exciting many more hot electrons compared to a bare Pt catalyst. The selectivity to MF was remarkably improved in Vac.-CeO_x/Pt than in Pristine-CeO_x/Pt and even O_2-CeO_x/Pt. Moreover, because hot electron generation efficiency was determined by total TOF and the partial oxidation selectivity, Vac.-CeO_x/Pt exhibited a significantly higher chemicurrent yield, owing to its improved TOF and selectivity compared to the others. This strongly confirmed that the enhanced crystallinity and low oxidation states of Vac.-CeO_x/Pt play a crucial role in enhancing selectivity and reaction-induced hot electron generation. According to our DFT-based reaction barrier calculations, the selectivity of MF was enhanced by the introduction of the heterogeneous interfaces and oxygen vacancies. We also found that the increase in the amount of the electron transfer by the oxygen vacancies is the origin of the low barrier of alkoxy hemiacetal formation. These two findings can rationalize the enhanced hot electron generation on Vac.-CeO_x/Pt.

In conclusion, we assessed the inherent role of the physicochemical properties of CeO_x in catalytic performance via precisely controlled reaction environments by fixed influential variables. Real-time detection of heterogeneous catalysis can be possible by observing the reaction-inducted hot electron directly in our unique Schottky nanodiode system. Furthermore, this TiO_2/Pt nanodiode successfully detects hot electrons generated through newly designed interfaces (CeO_x-Pt), demonstrating the potential to serve as a basic system for examining catalytic performance across various heterogeneous compositions. Our model platform combined with Schottky nanodiode is an effective and powerful technique to analyze the effects of materials with modified properties on chemical reactions, which suggests new design strategies for heterogeneous catalysts to accomplish efficient and desirable catalytic reactions. We believe that our strategy and findings can be applied to various heterogeneous catalysis fields where the chemical nature of constituting materials is critical to regulating reaction mechanisms.

Methods

Fabrication of 25 nm-wide line patterned master mold for nanowire transfer printing

Polystyrene-block-poly(dimethylsiloxane) (PS-b-PDMS) block copolymers with a molecular weight of 48 kg/mol and hydroxyl-terminated PDMS brush polymer with a molecular weight of 5 kg/mol were prepared (Polymer Source Inc.). KrF photolithography followed by a reactive ion etching process was used to create surface-patterned Si substrates which exhibit 1 μm pattern width and 1.2 μm period to guide the self-assembly of block copolymers. To prepare the hydrophobic surface-patterned Si substrate, the hydroxyl-terminated PDMS solution (in heptane solvent with a 2 wt%) was spin-casted onto the substrate, which was then thermally annealed at 150 °C and washed with heptane to remove residual polymer. PS-b-PDMS with a molecular weight of 48 kg/mol was dissolved in a mixed solvent of toluene, heptane, and PGMEA with a volume ratio of 1:1:1 with a 0.6–0.8 wt%. This PS-b-PDMS solution was spin-casted on the PDMS-treated Si substrates and subjected to solvent annealing with toluene vapor for 6-10 h at room temperature to form well-ordered line/space patterns. Following the solvent annealing, the substrates were etched to obtain oxidized PDMS nanostructures by using two-step processes of CF_4 and O_2 plasma treatment.

Fabrication of Pt film/TiO_2 Schottky nanodiodes

Using an electron-beam evaporator (A-tech system), the 150 nm of Ti film was deposited onto an n-type Si (100) wafer with 500 nm SiO_2 covered, which was separated by patterned shadow masks (4 × 7 mm^2) with deposition rates of 1.0 Å/s. After the deposition of Ti layers, thermal oxidation was conducted under 2 h 30 m at 510 °C to form n-type TiO_2. Then, ohmic contact pads with Ti (50 nm) and Au (50 nm) thin film were evaporated under patterned masks (5 × 5 mm^2) on two sides of the Schottky nanodevice to make an ohmic contact junction with deposition rates of 1.0 Å/s. Then, the Pt thin film (5 nm) was deposited by using top pad masks (3 × 6 mm^2) to make the Schottky junction of Pt/TiO_2 with a rate of 0.4 Å/ s. All metal films were evaporated in high-vacuum conditions of 2 × 10^{-7} Torr.

Fabrication of CeO_x nanowire arrays on Pt film/TiO_2 Schottky nanodiodes

The line-patterned master molds were pretreated by a hydroxyl-terminated PDMS brush which has hydrophobic properties. Then, on the top of the master mold, a poly (methyl methacrylate) (PMMA; MW = 100 kg/mol, Sigma Aldrich Inc.) solution which dissolved in a mixed solvent of toluene, acetone, and heptane with a volume ratio of 4.5:4.5:1 was spin-coated to form a polymer replica. Due to the hydroxyl-terminated PDMS brush treatment, the polymer replica was easily released from the master mold. A polyimide adhesive film (PI, 3 M Inc.) was then attached to the top surface of the polymer replica to detach the polymer replica from the master mold. Cerium oxide (CeO_2, iTASCO) was deposited through obliquely angled deposition (tilt angle: 80°) using an e-beam evaporator to form nanowire arrays on the detached polymer replica. After deposition, the cerium oxide nanowire arrays were transferred onto a target substrate (Cu foil or SiO_2) by exposing a mixed solvent vapor of acetone and heptane with a volume ratio of 1:1 at 55 °C for about 15 s and contacting with a target substrate. The PMMA polymer replica was removed by dipping into the toluene. After the transfer process, the cerium oxide nanowire arrays were annealed at 500 °C for two hours in various atmospheres (vacuum, Ar, and O_2) to form nanocrystalline non-stoichiometric CeO_x nanowires. Finally, the Cu foil and SiO_2 were wet-etched with a 0.1 M ammonium persulfate solution and a buffered oxide etchant (BOE, Sigma Aldrich Inc.) respectively, to transfer the nanocrystalline non-stoichiometric CeO_x nanowire arrays onto Pt film/TiO_2 Schottky nanodiodes.

Measurement of catalytic reaction and chemicurrent

A batch reactor chamber (1 L) was evacuated using turbomolecular pumps under a high-vacuum condition of 1 × 10^{-7} Torr for accurate quantitative analysis of catalytic methanol oxidation reaction. After the evacuation, the reaction chamber was filled with a gas mixture of methanol 4 Torr and oxygen 756 Torr at room temperature. Using a freeze-pump-thawing technique, the methanol was purified before the methanol vapor injection. All gas mixtures for catalytic reaction were recirculated with 2 L/min using the recirculation pump equipped with metal bellows for gas circulation in the batch reactor. After recirculation (1 h, 298 K) for equilibrium state, the methanol oxidation reaction was measured using gas chromatography (DS Science, iGC 7200 A) equipped with a flame ionization detector for detecting MF and methanol and with a thermal conductivity detector as a detector of CO_2. The calculation of Pt sites was obtained by geometrical assumptions, and reaction rates were calculated as TOF molecules/ (Pt sites * second), because there was no catalytic effect at 323–353 K in the methanol oxidation when only oxide nanowires existed. The current signals from the Schottky nanodiode under reactive conditions and non-reactive conditions were measured using an *I-V* instrument (Keithley Instrumentation, 2400 Source Meter) in the open circuit system that each ohmic pad (Au/Ti) on the Schottky nanodiode was connected with gold wires from the *I-V* instrument.

Characterization of materials

Structural and physicochemical characterization of the CeO_x/Pt were carried out with various techniques including SEM, TEM, XRD, XPS, and Probe station. The structural morphology of CeO_x nanowires and

CeO_x/Pt was investigated by field emission SEM (Hitachi, S-4800) and field emission TEM (FEI, Tecnai G2 F30 S-twin). The crystalline phases of the CeO_x nanowire arrays were analyzed using XRD (Rigaku, SmartLab) in θ–2θ scan mode using a Cu $K_{\alpha 1}$ incident beam with a scan range of 20–80°, a scan speed of 4° min^{-1}, and a step size of 0.01 Å. XPS (Thermo VG Scientific, K-Alpha) measurements were performed to investigate the chemical compositions and oxidation states of the CeO_x nanowires and the Pt film with an X-ray source of Al K-alpha (1486.3 eV) under ultra-high vacuum conditions. All the binding energies of XPS peaks were calibrated with a C1s peak at 284.8 eV. Raman measurements (Nanobase, XperRam S) were performed to investigate the oxidation states of the CeO_x nanowires and the Pt film using a laser wavelength of 532 nm, with gratings of containing 1800 grooves per 1 mm. All Raman signals were collected using 50x microscope lens. I–V characteristics (Keithley Instrumentation, 2400 Source Meter) of the CeO_x/Pt Schottky nanodiodes were obtained under mixtures of 4 Torr of methanol with O_2 to equal 760 Torr. By fitting the obtained I–V characteristics to the thermionic emission equation, a series resistance, Schottky barrier height, and ideality factor could be obtained.

DFT calculations

DFT calculations were performed using the plane-wave-basis Vienna ab initio simulation package (VASP) code with an energy cutoff of 400 eV[52,53]. The projector-augmented wave method was applied to treat core and valence electrons[54]. The generalized gradient approximation was used to describe the exchange-correlational interactions with the Perdew-Burke-Ernzerhof functional[55]. Geometries were fully relaxed until the maximum Hellmann–Feynman forces were less than 0.05 eV/Å, and the electronic structures were relaxed with a convergence criterion of 10^{-5} eV. To model the Pt film, we employed a (6 × 6) unit cell of Pt(111) surface with a three-atomic-layer thickness and a vacuum width of 15 Å. The bottom layer of the Pt slab was fixed to their bulk position. The Brillouin zone was sampled at the gamma point. To construct the CeO_2/Pt and Vac.-CeO_x/Pt systems, we combined tetrahedral $Ce_{10}O_{20}$ and $Ce_{10}O_{18}$ clusters with the modeled Pt film, as mentioned above. Based on the DFT-computed oxygen defect formation energies, the two oxygen vacancies were modeled at the perimeter interface (Supplementary Fig. 14). We adopted the Hubbard *U-J* value of 5 eV to describe the electronic properties of the ceria[56–58]. The Gibbs free energies were calculated according to the formula, $\Delta G = \Delta E_{ads} + \Delta E_{ZPE} - T\Delta S$ ($T = 300$ K), where ΔE_{ads}, ΔE_{ZPE}, and ΔS represent the changes in adsorption energy, zero-point energy, and entropy, respectively. The climbing image nudged elastic band method was employed to calculate the activation barriers[59]. The Bader charge analysis was performed to investigate the difference of the amount of charge transfer between the CeO_2/Pt and Vac.-CeO_x/Pt systems[60].

Data availability

All the data supporting the findings of this study are available within the article, its Supplementary Information/Source Data file. Additional details are available from the corresponding author upon request. Source data are provided with this paper.

References

1. Exner, K. S. Importance of the volcano slope to comprehend activity and selectivity trends in electrocatalysis. *Curr. Opin. Electrochem.* **39**, 101284 (2023).
2. Guo, X. Y. et al. Simultaneously achieving high activity and selectivity toward two-electron O-2 Electroreduction: The Power of Single-Atom Catalysts. *ACS Catal.* **9**, 11042–11054 (2019).
3. Wisniewska, J., Sobczak, I. & Ziolek, M. The effect of the calcium dopant on the activity and selectivity of gold catalysts supported on SBA-15 and Nb-containing SBA-15 in methanol oxidation. *Catal. Sci. Technol.* **11**, 2242–2260 (2021).
4. Lee, S. W. et al. Controlling hot electron flux and catalytic selectivity with nanoscale metal-oxide interfaces. *Nat. Commun.* **12**, 40 (2021).
5. Li, L. et al. Stable, active CO_2 reduction to formate via redox-modulated stabilization of active sites. *Nat. Commun.* **12**, 5223 (2021).
6. Shi, Q. Q. et al. CuO/TiO_2 heterojunction composites: an efficient photocatalyst for selective oxidation of methanol to methyl formate. *J. Mater. Chem. A* **7**, 2253–2260 (2019).
7. Lee, S. W. et al. Intrinsic relation between hot electron flux and catalytic selectivity during methanol oxidation. *ACS Catal.* **9**, 8424–8432 (2019).
8. Nienhaus, H. Electronic excitations by chemical reactions on metal surfaces. *Surf. Sci. Rep.* **45**, 1–78 (2002).
9. Gergen, B., Nienhaus, H., Weinberg, W. H. & McFarland, E. W. Chemically induced electronic excitations at metal surfaces. *Science* **294**, 2521–2523 (2001).
10. Gumhalter, B. Single-and multiphonon atom–surface scattering in the quantum regime. *Phys. Rep.* **351**, 1–159 (2001).
11. Mantell, D. et al. The exciting oxidation of CO on Pt. *Chem. Phys. Lett.* **81**, 185–187 (1981).
12. Frischkorn, C. & Wolf, M. Femtochemistry at metal surfaces: nonadiabatic reaction dynamics. *Chem. Rev.* **106**, 4207–4233 (2006).
13. Park, J. Y., Baker, L. R. & Somorjai, G. A. Role of hot electrons and metal–oxide interfaces in surface chemistry and catalytic reactions. *Chem. Rev.* **115**, 2781–2817 (2015).
14. Hasselbrink, E. How non-adiabatic are surface dynamical processes? *Curr. Opin. Solid State Mat. Sci.* **10**, 192–204 (2006).
15. Wodtke, A. M., Matsiev, D. & Auerbach, D. J. Energy transfer and chemical dynamics at solid surfaces: The special role of charge transfer. *Prog. Surf. Sci.* **83**, 167–214 (2008).
16. Park, J. Y., Kim, S. M., Lee, H. & Nedrygailov, I. I. Hot-electron-mediated surface chemistry: toward electronic control of catalytic activity. *Acc. Chem. Res.* **48**, 2475–2483 (2015).
17. Nienhaus, H. et al. Electron-hole pair creation at Ag and Cu surfaces by adsorption of atomic hydrogen and deuterium. *Phys. Rev. Lett.* **82**, 446–449 (1999).
18. Oh, S. et al. Effect of the metal-support interaction on the activity and selectivity of methanol oxidation over Au supported on mesoporous oxides. *Chem. Commun.* **54**, 8174–8177 (2018).
19. Reddy, K. P. et al. The facet effect of ceria nanoparticles on platinum dispersion and catalytic activity of methanol partial oxidation. *Chem. Commun.* **57**, 7382–7385 (2021).
20. Frey, H. et al. Dynamic interplay between metal nanoparticles and oxide support under redox conditions. *Science* **376**, 982–987 (2022).
21. Zhou, J. et al. Interfacial compatibility critically controls Ru/TiO_2 metal-support interaction modes in CO_2 hydrogenation. *Nat. Commun.* **13**, 327 (2022).
22. Bai, S. T. et al. Homogeneous and heterogeneous catalysts for hydrogenation of CO_2 to methanol under mild conditions. *Chem. Soc. Rev.* **50**, 4259–4298 (2021).
23. Navarro-Jaen, S. et al. Highlights and challenges in the selective reduction of carbon dioxide to methanol. *Nat. Rev. Chem.* **5**, 564–579 (2021).
24. Song, H. C. et al. Engineering nanoscale interfaces of metal/oxide nanowires to control catalytic activity. *ACS Nano* **14**, 8335–8342 (2020).
25. Choi, Y. et al. Unravelling inherent electrocatalysis of mixed-conducting oxide activated by metal nanoparticle for fuel cell electrodes. *Nat. Nanotechnol.* **14**, 245–251 (2019).

26. Craciun, R., Daniell, W. & Knözinger, H. The effect of CeO_2 structure on the activity of supported Pd catalysts used for methane steam reforming. *Appl. Catal. A-Gen.* **230**, 153–168 (2002).
27. Cargnello, M. et al. Control of metal nanocrystal size reveals metal-support interface role for ceria catalysts. *Science* **341**, 771–773 (2013).
28. Kropp, T. & Paier, J. Reactions of methanol with pristine and defective ceria (111) surfaces: a comparison of density functionals. *J. Phys. Chem. C.* **118**, 23690–23700 (2014).
29. Van Deelen, T. W., Mejía, C. H. & De Jong, K. P. Control of metal-support interactions in heterogeneous catalysts to enhance activity and selectivity. *Nat. Catal.* **2**, 955–970 (2019).
30. Kim, Y. J., Lee, G. R., Cho, E. N. & Jung, Y. S. Fabrication and applications of 3D nanoarchitectures for advanced electrocatalysts and sensors. *Adv. Mater.* **32**, 1907500 (2020).
31. Lee, G. R. et al. Efficient and sustainable water electrolysis achieved by excess electron reservoir enabling charge replenishment to catalysts. *Nat. Commun.* **14**, 5402 (2023).
32. Ahn, J. et al. Illuminating recent progress in nanotransfer printing: core principles, emerging applications, and future perspectives. *Adv. Sci.* **11**, 2303704 (2024).
33. Han, H. J. et al. Unconventional grain growth suppression in oxygen-rich metal oxide nanoribbons. *Sci. Adv.* **7**, eabh2012 (2021).
34. Jeong, J. W. et al. High-resolution nanotransfer printing applicable to diverse surfaces via interface-targeted adhesion switching. *Nat. Commun.* **5**, 5387 (2014).
35. Park, T. W. et al. Thermally assisted nanotransfer printing with sub–20-nm resolution and 8-inch wafer scalability. *Sci. Adv.* **6**, eabb6462 (2020).
36. Chen, J.-C., Chen, W.-C., Tien, Y.-C. & Shih, C.-J. Effect of calcination temperature on the crystallite growth of cerium oxide nano-powders prepared by the co-precipitation process. *J. Alloy. Compd.* **496**, 364–369 (2010).
37. Choudhury, B., Chetri, P. & Choudhury, A. Oxygen defects and formation of Ce^{3+} affecting the photocatalytic performance of CeO_2 nanoparticles. *RSC Adv.* **4**, 4663–4671 (2014).
38. Choudhury, B., Chetri, P. & Choudhury, A. Annealing temperature and oxygen-vacancy-dependent variation of lattice strain, band gap and luminescence properties of CeO_2 nanoparticles. *J. Exp. Nanosci.* **10**, 103–114 (2015).
39. Guo, M. et al. UV and visible raman studies of oxygen vacancies in rare-earth-doped ceria. *Langmuir* **27**, 3872–3877 (2011).
40. Bunaciu, A. A., Udriştioiu, E. G. & Aboul-Enein, H. Y. X-Ray diffraction: instrumentation and applications. *Crit. Rev. Anal. Chem.* **45**, 289–299 (2015).
41. Jeon, B., Lee, H., Goddeti, K. C. & Park, J. Y. Hot electron transport on three-dimensional Pt/mesoporous TiO_2 schottky nanodiodes. *ACS Appl. Mater. Interfaces* **11**, 15152–15159 (2019).
42. Lee, H. et al. Graphene–semiconductor catalytic nanodiodes for quantitative detection of hot electrons induced by a chemical reaction. *Nano Lett.* **16**, 1650–1656 (2016).
43. Hervier, A., Baker, L. R., Komvopoulos, K. & Somorjai, G. A. Titanium oxide/platinum catalysis: charge transfer from a titanium oxide support controls activity and selectivity in methanol oxidation on platinum. *J. Phys. Chem. C.* **115**, 22960–22964 (2011).
44. Zafeiratos, S. et al. Methanol oxidation over model cobalt catalysts: Influence of the cobalt oxidation state on the reactivity. *J. Catal.* **269**, 309–317 (2010).
45. Wittstock, A. et al. Nanoporous gold catalysts for selective gas-phase oxidative coupling of methanol at low temperature. *Science* **327**, 319–322 (2010).
46. Hervier, A., Renzas, J. R., Park, J. Y. & Somorjai, G. A. Hydrogen oxidation-driven hot electron flow detected by catalytic nanodiodes. *Nano Lett.* **9**, 3930–3933 (2009).
47. Lee, H. et al. Chemical-reaction-induced hot electron flows on platinum colloid nanoparticles under hydrogen oxidation: impact of nanoparticle size. *Angew. Chem. -Int. Ed.* **54**, 2340–2344 (2015).
48. Lee, H. et al. Boosting hot electron flux and catalytic activity at metal–oxide interfaces of PtCo bimetallic nanoparticles. *Nat. Commun.* **9**, 2235 (2018).
49. Li, Y. et al. What Changes on the inverse catalyst? insights from CO oxidation on Au-supported ceria nanoparticles using Ab initio molecular dynamics. *ACS Catal.* **10**, 3164–3174 (2020).
50. Xu, B. et al. Theoretical study of O-assisted selective coupling of methanol on Au(111). *J. Phys. Chem. C.* **115**, 3703–3708 (2011).
51. Zhong, W. et al. The O, OH and OOH-assisted selective coupling of methanol on Au–Ag(111). *Phys. Chem. Chem. Phys.* **18**, 9969–9978 (2016).
52. Kresse, G. & Furthmüller, J. Efficient iterative schemes for ab initio total-energy calculations using a plane-wave basis set. *Phys. Rev. B* **54**, 11169–11186 (1996).
53. Kresse, G. & Joubert, D. From ultrasoft pseudopotentials to the projector augmented-wave method. *Phys. Rev. B* **59**, 1758–1775 (1999).
54. Blöchl, P. E. Projector augmented-wave method. *Phys. Rev. B* **50**, 17953–17979 (1994).
55. Perdew, J. P., Burke, K. & Ernzerhof, M. Generalized gradient approximation made simple. *Phys. Rev. Lett.* **77**, 3865–3868 (1996).
56. Dudarev, S. L. et al. Electron-energy-loss spectra and the structural stability of nickel oxide: An LSDA+U study. *Phys. Rev. B* **57**, 1505–1509 (1998).
57. Kim, H. Y., Lee, H. M. & Henkelman, G. CO oxidation mechanism on CeO_2-supported Au nanoparticles. *J. Am. Chem. Soc.* **134**, 1560–1570 (2012).
58. Andersson, D. A. et al. Modeling of CeO_2, Ce_2O_3, and CeO_2–X in the LDA+U formalism. *Phys. Rev. B* **75**, 035109 (2007).
59. Henkelman, G., Uberuaga, B. P. & Jónsson, H. A climbing image nudged elastic band method for finding saddle points and minimum energy paths. *J. Chem. Phys.* **113**, 9901–9904 (2000).
60. Tang, W., Sanville, E. & Henkelman, G. A grid-based Bader analysis algorithm without lattice bias. *J. Phys. -Condes. Matter* **21**, 084204 (2009).

Acknowledgements

This work was supported by Korea Institute of Energy Technology Evaluation and Planning (KETEP) grant funded by the Korean government (MOTIE) (No. 20214000000650, Energy Innovation Research Center for Fuel Cell Technology), National Research Foundation of Korea (NRF) grant funded by the Korean government (MSIT) (2022R1A2C3004242), and the National Research Foundation of Korea funded by the Ministry of Science and ICT (RS-2024-00450102).

Author contributions

G.R.L., K.S., Y.S.J., and J.Y.P. conceived the project. G.R.L. and K.S. conducted the overall sample preparation, device fabrication, measurements, and analyses. D.H., M.K., and D.K. performed the DFT calculations and theoretical analyses. G.R.L., K.S., J.A., and Y.R. optimized the sample preparation, device fabrication, and catalytic performance measurements. G.R.L. and Y.S.J. led the discussion and wrote the manuscript with input from all authors. J.Y.P., Y.S.J., and D.K. supervised the project. All authors discussed the results and contributed to the manuscript.

Competing interests

The authors declare no competing interests.

Additional information

Supplementary information The online version contains supplementary material available at https://doi.org/10.1038/s41467-025-57946-9.

Correspondence and requests for materials should be addressed to Donghun Kim, Yeon Sik Jung or Jeong Young Park.

Peer review information *Nature Communications* thanks Xiaorui Zheng and the other, anonymous, reviewer(s) for their contribution to the peer review of this work. A peer review file is available.